J. Fluid Mech. (1972), *vol.* 52, *part* 3, *pp.* 543–563
Printed in Great Britain

Some effects of intense turbulence on the aerodynamics of a circular cylinder at subcritical Reynolds number

By DAVID SURRY
Institute for Aerospace Studies, University of Toronto†

(Received 3 July 1971)

The effect of high intensity large-scale free-stream turbulence on the flow past a rigid circular cylinder has been studied experimentally at subcritical Reynolds numbers. Grids were used to produce homogeneous turbulence fields with longitudinal scales ranging from 0·36 to 4·40 cylinder diameters and with longitudinal intensities greater than 10%. Power and cross-spectra of the turbulence components (the 'system input') have been measured in order to carefully define the turbulence characteristics.

In the response experiments, a special model measured arbitrary two-point pressure correlations. Subsequent integrations yielded the spectral properties of the unsteady lift and drag. Measurements of mean drag and Strouhal frequency indicate that to some extent even severe large-scale turbulence can be considered to be qualitatively equivalent to an increase in the effective Reynolds number. Vortex shedding is not seriously disrupted by severe turbulence, but is affected more by low than by high frequencies. The unsteady lift response is still dominated by the vortex shedding, whereas the unsteady drag becomes primarily a response to turbulence. The cross-spectra of the drag forces for the one turbulence case examined overlay well when plotted against lateral separation divided by wavelength. This has enabled a 'describing function' for the drag response to turbulence to be derived. This describing function is the central element needed for the calculation of the structural response of such cylinders in the drag direction.

1. Introduction

In recent years, the desire for more realistic design criteria for both earth-fixed structures and aircraft has focused increasing attention on the prediction of the response of such structures to atmospheric turbulence. There are basically two major weaknesses in the current predictive methods. First, improvements in the description of the atmospheric wind environment must be made and, second, the relation between the turbulent inputs to a body and the forces and pressures on that body must be determined more accurately. The experiment to be discussed has been designed to help elucidate this second problem. As a first step, a rigid circular cylinder has been subjected to relatively homogeneous and intense turbulence. The circular cylinder provides an attractive geometry for

† Present address: Faculty of Engineering Science, University of Western Ontario, London, Ontario.

study both because of its fundamental, and aerodynamically classical, nature and because of its common occurrence in engineering structures such as chimneys and rocket boosters.

Theoretical response studies of slender cylindrical structures to a turbulent wind have been considered in the past (e.g. Davenport 1962; Etkin 1966), however, a major assumption in the methods is made about the relationship between the relative wind and the force on the body. The work described here was intended as an experimental examination of this relationship; also, by its nature it has provided some detailed information about the fluctuating pressure field on the cylinder. This work is described in detail in Surry (1969). The following is intended to give a brief description of the experiment and the major results.

2. Apparatus and method

The low-speed closed-circuit wind tunnel used in the experiments allows speeds up to 60 m/s to be attained through the empty 122 × 81 cm test section. The turbulent inputs to the cylinder model were produced by three different coarse biplane grids. (Details of the grid design and development can be found in Surry (1969).) Owing to the shortness of the test section available, both the model and the grids were mounted in the first diffuser after the test section (5° expansion), causing a small adverse pressure gradient of the order of 0·5 % of the dynamic pressure per diameter across the model. This is not considered to have significantly affected the turbulence response results although it may have caused slightly premature separation.

The 3·15 cm diameter cylinder model is shown schematically in figure 1. The model spanned the wind tunnel but was isolated from it by passing through

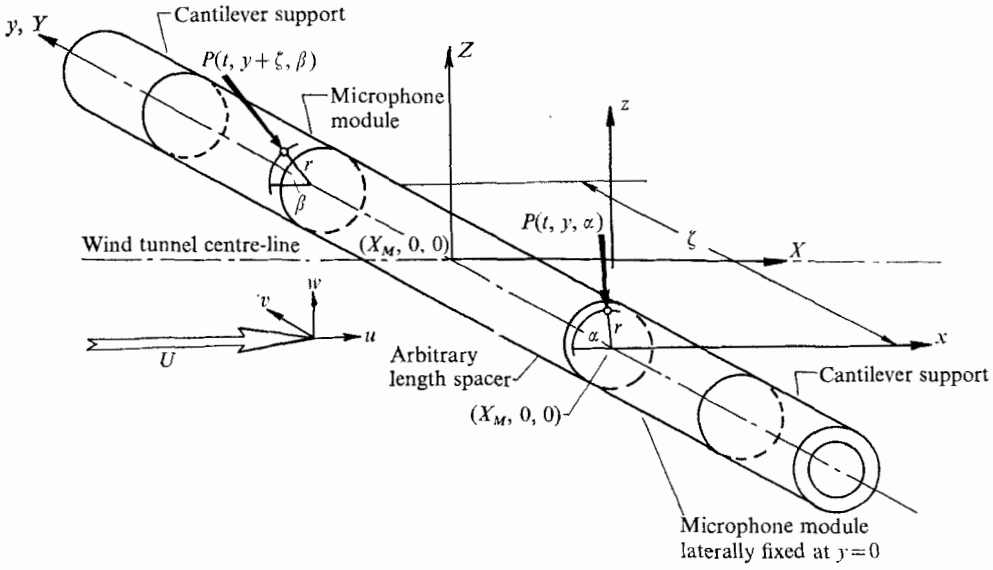

FIGURE 1. Schematic diagram of the cylinder in the airstream. $X = x = 0$ is located at the grid plane.

elaborate wall seals onto heavy vibration-isolating end supports outside the tunnel. The model span was 60 diameters. Measured acceleration at the centre of the model under turbulent test conditions indicated a root-mean-square displacement of less than 3×10^{-4} diameters. The model consisted of two opposing cantilevers, each supporting a pressure measuring module with an arbitrary length spacer between them, the complete cylinder being held together by a compressive end load. Each module was a section of the cylinder containing a Bruel & Kjaer one inch condenser microphone, which sensed the pressure at a point on the surface through a 0·159 cm diameter hole. The cylindrical geometry thus allowed pressure correlations between any two arbitrary points to be obtained. The microphone systems were modified to extend the pressure response at low frequencies. The resulting system was flat down to 7 Hz and was 3 db down at 2 Hz. The total system, including the microphone modules, was calibrated for amplitude response and phase difference. The modules introduced a resonance at 950 Hz and some nonlinearity above 800 Hz for the larger experimental pressure amplitudes obtained. Below 800 Hz (corresponding to $fD/\overline{U} \simeq 1{\cdot}6$, where f is frequency, D is cylinder diameter and $\overline{U}$ is mean velocity) the data could be accurately corrected for amplitude response. In this range, the phase difference between the two systems was less than two degrees.

To obtain the statistical properties of the model's fluctuating lift and drag it was necessary to measure sufficient two-point pressure correlations to adequately determine the following integrals:

$$\left.\begin{aligned} R_{ll}(\tau,\zeta) &= \frac{D^2}{4}\int_0^{2\pi}\int_0^{2\pi} R_{pp}(\tau,\zeta,\alpha,\beta)\sin\alpha\,\sin\beta\,d\alpha,d\beta, \\ R_{dd}(\tau,\zeta) &= \frac{D^2}{4}\int_0^{2\pi}\int_0^{2\pi} R_{pp}(\tau,\zeta,\alpha,\beta)\cos\alpha\,\cos\beta\,d\alpha\,d\beta, \end{aligned}\right\} \tag{1}$$

where R_{pp}, R_{ll} and R_{dd} are cross-correlations (see below) of unsteady surface pressure, sectional lift and sectional drag, respectively, between two lateral stations a distance ζ apart; τ is a time delay and α and β are azimuthal angles, as defined in figure 1. Stationarity and homogeneity have been assumed. In practice, a matrix of pressure cross-correlations was measured for 15° increments of α and β around the cylinder, where $R_{pp}(\tau,\zeta,\alpha,\beta) = \langle p(t,y,\alpha)\,p(t+\tau,y+\zeta,\beta)\rangle$, $\langle\ \rangle$ denoting an ensemble average, which in the present circumstances is equal to the time average. With the additional assumption of symmetry, the minimum number of unique angle pairs for a given lateral spacing can be shown to be N^2+N+1, where $N = \pi/\Delta\theta$ and $\Delta\theta$ is the angular increment used (in radians). In this case 157 angle pairs were examined for each lateral spacing. Each pair provided a pressure cross-correlation as a function of time delay. This data was obtained on-line on punched cards using a Princeton Applied Research Model 100 Signal Correlator. This provided correlation estimates for 100 equi-spaced values of τ.

The flow's velocity characteristics were measured using linearized constant-temperature hot-wire anemometer techniques. Spectra of the three turbulence components, and some surface pressure spectra, were obtained using an

alternative technique whereby the analog signals were first recorded and then digitally sampled and processed.

In all, four flow fields were examined: three grid cases and the empty tunnel. However, lift and drag cross-spectra were only obtained for the largest scale and intensity case. The cases are numbered in order of grid bar width as 0 (empty tunnel), 1, 3 and 4. An intermediate case 2 had to be abandoned owing to an acoustic resonance discovered at the pressure measuring stage.

3. Flow measurements at the model station

The properties of the flows were examined in some detail along the eventual location of the model centre-line to determine the best lateral location for the measurement region. An 'influence region' was arbitrarily taken as equal to the maximum separation intended between the pressure modules ($10D$) plus twice

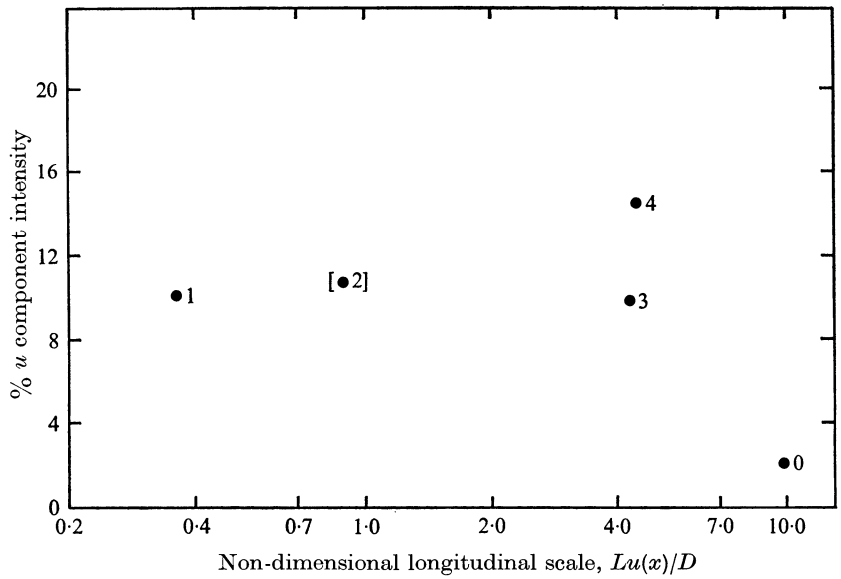

FIGURE 2. Summary of the longitudinal scale and intensity of the u component for the flow fields examined. The numbers designate the grids in order of bar size.

the distance required for the lateral correlation of the largest scale case to become zero. Since this latter distance was also found to be approximately $10D$, flow measurements were concentrated over a central $30D$ influence region. For all four turbulence cases the mean velocity is within $\pm 5\,\%$ of the median over this range. The turbulence component intensities are constant to within $\pm 7\,\%$ for the three grid cases. The empty tunnel suffered from poor flow in the diffuser and, as a result, the turbulence levels show sharp rises within the influence region but outside the central region over which the modules actually traversed. Figure 2 summarizes the mean values of the major parameters for the four flow cases examined. These are the percentage intensity ($100\bar{\bar{u}}/\overline{U}$, where $\bar{\bar{u}}$ denotes the r.m.s. value of $u(t)$) and the longitudinal scale of the u component ($Lu(x)$). In

this graph the longitudinal scale was obtained by integrating the normalized autocorrelation function of the u component to yield a longitudinal time scale; then the longitudinal length scale $Lu(x)$ of the u component in the x direction was determined simply by multiplying by $\overline{U}$, the mean velocity. The cross-component intensities were also measured and found to be typically 20% less than the u component values.

4. Pressure measurements on the cylinder surface

Static pressures

For each of the four cases static pressure distributions were recorded by connecting the pressure-sensing module to a Betz manometer. These distributions are shown in figure 3 plotted against a reference angle θ'. In the figure, Re is the Reynolds number based on the mean velocity $\overline{U}$ and the cylinder diameter, S is the Strouhal number and T is the Taylor parameter $(\bar{\bar{u}}/\overline{U})\,[D/Lu(y)]^{0\cdot2}$. $\theta' = 0$ corresponds approximately to the first stagnation point. In fact, the symmetry of the zero crossings of the static pressure distributions was used to determine the value of θ' corresponding to the exact stagnation point. Two sets of data were obtained for two lateral locations. No attempt has been made to correct the results for the longitudinal static pressure gradient. It can be seen that for the three grid cases the two lateral stations repeat very well; however, the empty tunnel shows the effect of poor flow across the model.

The pressure distributions show stagnation pressure coefficients greater than unity. For cases 0, 3 and 4 respectively the three maximum stagnation pressures recorded were 1·062, 1·024 and 1·062. (It should be pointed out that the reference static pressure used in these results was obtained by manifolding eight wall taps at the model location. However, for case 1 these taps were in the near wake of the grid supports and hence, for this case only, the reference static pressure was defined so as to force the data through the average of the other three stagnation pressures, i.e. $C_p = 1{\cdot}049$. This does not alter the basic shape properties or the integrated pressure drag coefficient.) That the stagnation pressure coefficient is greater than unity is expected in a turbulent flow, but the precise relation between the stagnation pressure and the turbulent stream is uncertain (see Hinze 1959). If the total velocity vector were assumed to be stagnated, the values for cases 0, 3 and 4 would be expected to be 1·003, 1·024 and 1·050. It would be unwise to compare the numerical values in detail and to draw any positive conclusion about the stagnation pressures obtained as in all cases there is some doubt as to the absolute accuracy of such wall pressure measurements in turbulent flow. It is probable, though, that the high measured value in the empty diffuser again mirrors the poor flow condition near the walls.

It is also evident from the pressure distributions of figure 3 that significant changes occur owing to the presence of turbulence, since all four cases are within 15% of a Reynolds number of 40000. Furthermore, a comparison between cases 1 and 3 shows the significant role that scale plays at constant turbulent intensity. Unfortunately, the circular cylinder's lack of fixed separation points makes it difficult to identify what might naïvely be thought of as two separate

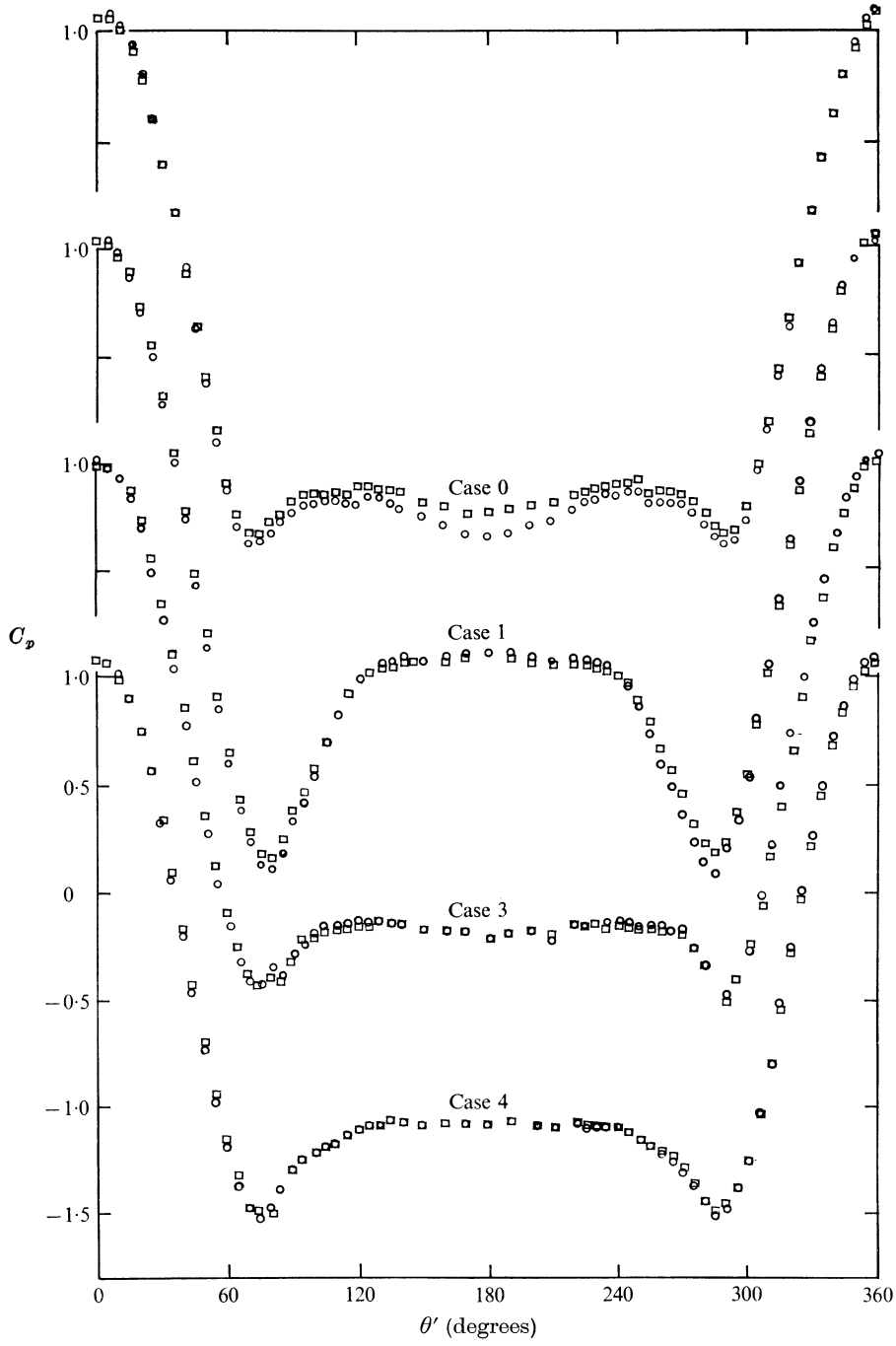

FIGURE 3. Mean pressure distributions around the cylinder circumference. □, $y/d = 0$; ○, $y/d = 9{\cdot}8$.

Case	$Lu(x)/D$	$\bar{u}/U$	Re	S	C_d	T
0	9·8	0·025	$4{\cdot}42 \times 10^4$	0·19	1·31	0·015
1	0·36	0·105	$3{\cdot}54 \times 10^4$	0·22	0·93	0·161
3	4·3	0·100	$3{\cdot}62 \times 10^4$	0·19	1·23	0·088
4	4·4	0·147	$3{\cdot}38 \times 10^4$	0·20	1·14	0·123

aspects of the turbulent interaction: the first being a direct effect on the boundary layer which leads to changes in the position of the separation points and the second being an effect on the flow outside the boundary layer, including the wake. In reality one would expect these two effects to be coupled. The boundary-layer interaction has provided the basis for the concept of an effective Re since free-stream turbulence tends to promote boundary-layer characteristics normally

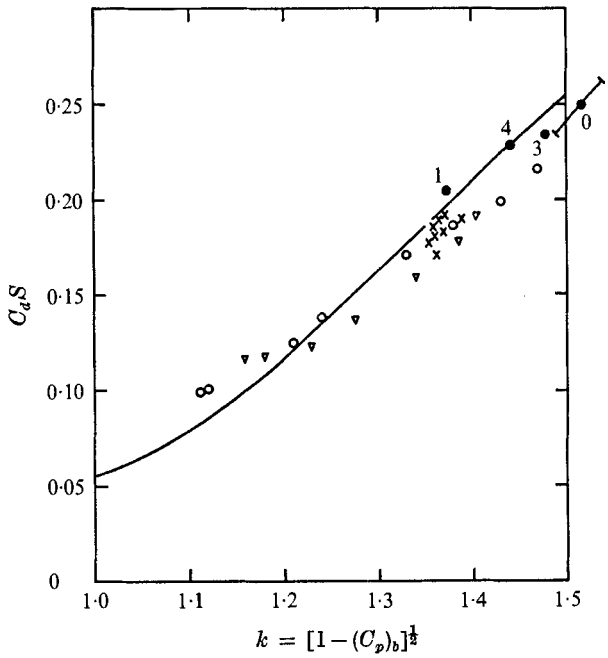

FIGURE 4. Drag coefficient × Strouhal number versus the base pressure parameter k. ×, Roshko (1961), high Re; ○, cylinder without grid; ▽, cylinder with grid; —, theoretical curve, Bearman (1967); ●, present results.

associated with higher Re. For instance, Bearman (1968, 1969) related the properties of the turbulence to the critical Reynolds number by means of the Taylor parameter. From the present results, only particular single Re values of integrated pressure drag and Strouhal number are available, but it can at least be said that the Taylor parameter orders the results logically. As it increases, implying an increase in effective Re, so does S. Furthermore, the mean pressure distributions change consistently towards those associated with higher Re (cf. Fage & Falkner 1931) and the drag coefficients decrease. All these trends are consistent with an effective Re increasing towards a value of about 2×10^5 associated with case 1.

It is also interesting to note that even under the intense turbulent flow conditions investigated here, the relation between C_d, S and base pressure suggested by Bearman (1967) still holds. This is shown in figure 4, which is taken from Bearman's (1968) paper with the present data added, the base pressure used being simply the 'rear stagnation' value. The best agreement is obtained for the two pressure distributions having relatively constant wake pressure (cases 1

and 4) and improved agreement would be obtained for cases 0 and 3 if an average base pressure were used.

Power spectra

Power spectra of the surface pressure fluctuations were obtained for 30° increments around the model. An example of the results corrected for system frequency response is given in figure 5. They are presented as mean curves obtained from a number of data sets. These are all at 150° from the front stagnation point and

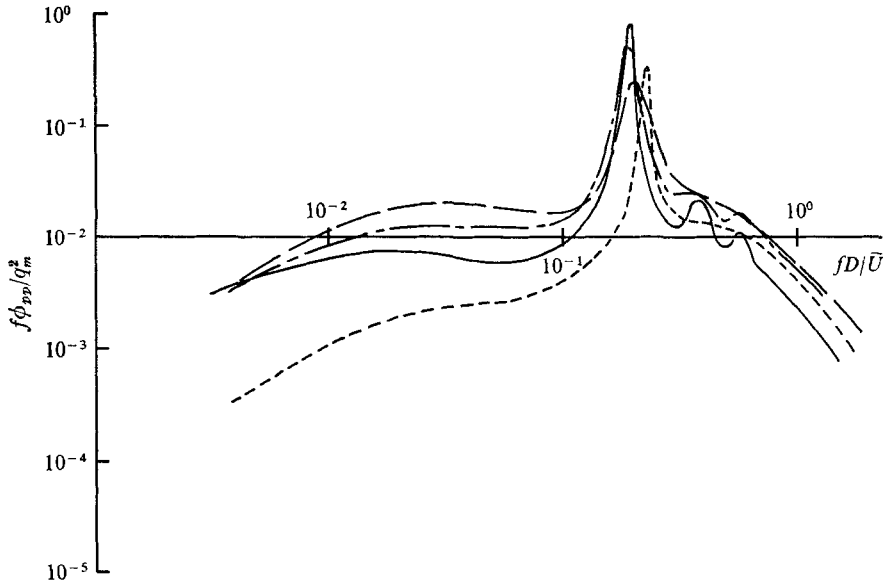

FIGURE 5. Surface pressure spectra at 150° from the front stagnation point. ——, case 0; – – – –, case 1; —·—, case 3; — —, case 4.

are plotted in a dimensionless form $f\phi_{pp}/q_m^2$, where q_m is the dynamic pressure at the model station, f is frequency and ϕ_{pp} is the one-sided pressure power spectrum $\left(\int_0^\infty \phi_{pp}\,df = \overline{p^2}\right)$. The low frequency data is as one would expect, assuming some simple relation between the turbulence and pressure at these frequencies. The two highest curves at low frequency correspond to the large-scale grids in order of intensity. The lowest curve is the small-scale input, where the energy is concentrated at the high frequency end. The intermediate curve gives the rather 'dirty' large-scale empty-tunnel results. The effects of turbulence on the shedding peak, apart from the slight changes in S, are primarily a broadening and lowering. It is difficult to assess how much of these effects is due to the changes in mean properties commented on previously, but it does seem to be clear that the large-scale inputs (3 and 4) tend to broaden the peak, whereas similar intensities with a smaller scale (1) produce no noticeable broadening over the 'dirty' empty-tunnel case (0).

Also of interest in this data is the appearance of the second harmonic of the shedding which is visible for the larger scale, lower intensity cases, the empty tunnel ($10D$, 2 %) and case 3 ($4D$, 10 %).

Root-mean-square pressures

Figure 6 shows the distribution of r.m.s. fluctuating pressure around the cylinder in the four cases. (These results are uncorrected for module response, but this source of error was examined using the corrected spectral distributions and found

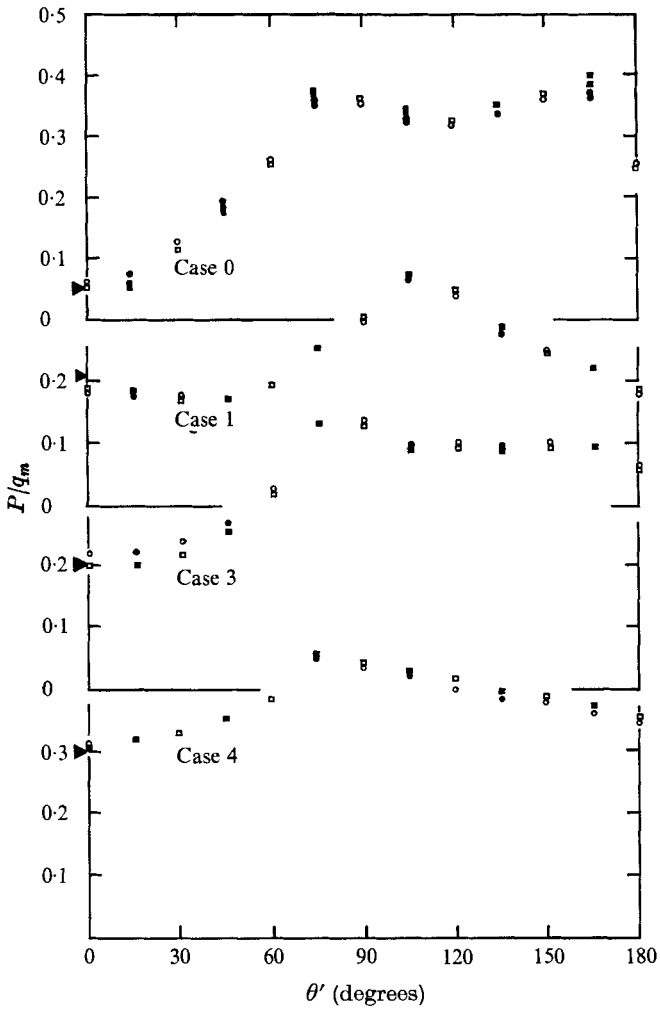

FIGURE 6. Root-mean-square fluctuating pressure distributions around the cylinder circumference. ■, fixed module single datum; □, fixed module averaged data; ●, moveable module single datum; ○, moveable module averaged data; ▶, $2\bar{u}/\bar{U}$.

to be less than $\pm 5\,\%$ except in the case of wake regions for case 1 where the error may rise to about $+10\,\%$.) The r.m.s. pressures show marked changes between turbulent inputs. In particular, at the front stagnation point the r.m.s. pressures are in good agreement with those expected assuming the simple linearization $p(t) = \rho \bar{U} u(t)$, where ρ is the air density, i.e. $\bar{\bar{p}}/q_m = 2\bar{\bar{u}}/\bar{U}$. For the empty-tunnel case 0, the vortex shedding causes the r.m.s. pressures to increase with θ' until

separation occurs. The levels of the surface pressure remain high in the wake region although power spectra indicate that the broad-band fluctuations in the wake now markedly contribute. At the rear stagnation point the contribution from the shedding energy decreases sharply, most of the energy being due to the wake turbulence. The secondary rise in the wake at $\theta' = 150°$ may be attributed to secondary circulation and corresponds to the well-defined change in static pressures over the wake region shown in figure 3. It is notable for case 1 that there is a drop in r.m.s. pressure levels from the front stagnation point, that the peak pressures are moved rearward (corresponding to the movement of the separation point) and that the wake levels decrease uniformly to a lower value of rear pressure than that found for the empty tunnel. This all indicates that the prime effect of the higher turbulence level in this case is to change the mean flow characteristics, and hence also its fluctuating characteristics, rather than being a direct superposition of effects. The r.m.s. pressure distributions for the larger scale cases 3 and 4, however, both appear more nearly uniform over the cylinder surface, with the higher intensity case giving a closer approach to uniformity. Furthermore in neither case is there a sharp drop in level at the rear stagnation point.

Lateral pressure scales

Whereas the power spectra of figure 5 suggested that large-scale turbulence interferes with the phase coherence of the shedding, the spatial coherence of the flow can be determined by two-point lateral correlations at zero time delay. Two lateral scales determined by integrating such correlations are shown in figure 7 as functions of circumferential angle. Interpretation of the scales determined from the complete pressure signal (giving Lp) in figure 7(*a*) are complicated by the pressure response originating from the turbulence. (In fact they tend to mirror the input turbulence scale.) Hence, a narrow-band correlation length (Lp_s) was found, corresponding to the coherence exhibited at the shedding peak alone. This latter scale is then an upper bound on the scale associated with vortex shedding. In practice, the narrow-band correlations were derived from the ratio of cross-spectrum to power-spectrum, which for any particular pair of lateral stations will exhibit peak coherence at the vortex shedding frequency. When these estimates for the narrow-band correlation of the vortex shedding are plotted against the lateral spacing they can be fitted very well by a curve of the form

$$\gamma_s = \exp\{-(b_s\eta)^{1\cdot4}\}, \tag{2}$$

where b_s is an arbitrary parameter, and $\eta = f\zeta/\overline{U}$. This expression was numerically integrated to provide a measure of scale, $Lp_s/\lambda_s \equiv \int_0^\infty \gamma_s \, d\eta$. This lateral correlation is shown non-dimensionalized by the wavelength associated with the shedding, $\lambda_s = \overline{U}/f_s$. Also shown are the Strouhal numbers measured, which are essentially D/λ_s.

In figure 7(*b*) a typical scatter bar is shown on one of the empty-tunnel measurements. It can be seen that the narrow-band lateral correlation is reduced in the presence of turbulence, and in all cases a sharp drop at the rear of the

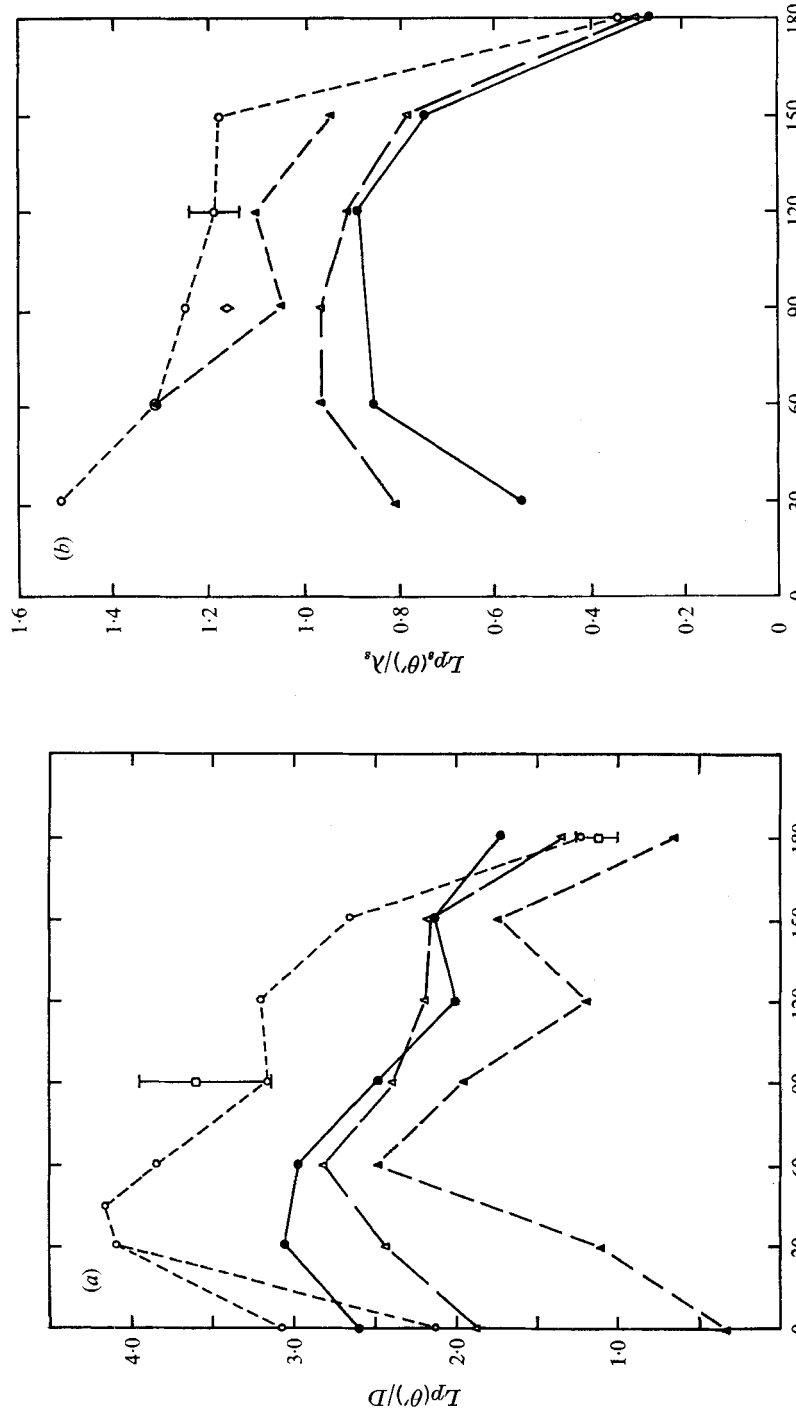

FIGURE 7. Lateral pressure scales (*a*) of the total fluctuating pressure response (*b*) of the narrow-band vortex shedding. ○, case 0, $S = 0{\cdot}19$; ▲, case 1, $S = 0{\cdot}22$; △, case 3, $S = 0{\cdot}19$; ●, case 4, $S = 0{\cdot}20$; □, Prendergast (1958), $Re = 4{\cdot}7 \times 10^4$; ◇, El Baroudi (1960), $Re \sim 4{\cdot}5 \times 10^4$.

cylinder is seen. (The correlation length at 180° is presented in terms of λ_s, although the oscillating pressure occurs at $2f_s$.) In terms of wavelengths at least (see figure 7*b*), the small-scale input case 1 is virtually as well correlated as the empty-tunnel case 0, again indicating that the prime interaction at this small scale is with the boundary layer, as was also suggested by the power spectra. Also shown are two lateral correlation length measurements found by other workers in smooth flow.

Prendergast (1958) measured pressure correlations which did not asymptote to zero. His corrected value agrees reasonably well with the value found here in rather 'dirty' flow; however, this may be fortuitous as here the background turbulence would be expected to reduce the measured correlation. It follows that Lp_s/D for this case is substantially larger, of order 6·0. It is interesting to note that this narrow-band value agrees quite well with El Baroudi's later measurement (1960). El Baroudi repeated Prendergast's experiment using hot-wire probes near the cylinder and did not have non-zero asymptotes. El Baroudi's data is plotted on the Lp_s/λ_s graph using $S = 0{\cdot}185$ and his value of $Lp/D = 6{\cdot}3$ at $Re = 4{\cdot}5 \times 10^4$. It might be noted that experimental discrepancies as to the correlation length over this Re range still exist.

5. Pressure–velocity describing functions

For the particular case of the front stagnation point, the simple linearized relationship between the fluctuating pressure and the u component of velocity was investigated further by forming the ratio of their power spectra, ϕ_{pp}/ϕ_{uu}. For the simple case $p(t) = \rho\overline{U}\,u(t)$, $\phi_{pp}/\rho^2\overline{U}^2\phi_{uu}$ should be unity. The results for the four cases examined are shown in figure 8. It is interesting to note that the data is generally high at low frequency which might be expected, owing to the neglect in the simple analysis of cross-components, acceleration effects and the pressure field of the cylinder itself. The rapid drop-off in pressure response at high frequency is similar in all four cases, with a slope of about $-1{\cdot}5$, and indicates a frequency above which the free-stream turbulence has negligible effect on the flow field of the cylinder, at least near the stagnation point. The rapid drop-off in response begins at about $D/\lambda = 0{\cdot}3$ which is similar to the observed break point for the admittance of square plates as reported in Bearman (1970).

6. Fluctuating drag and lift

Root-mean-square lift and drag coefficients and lateral scales

Sufficient pressure correlations to allow integration of equations (1) were only measured for case 4 (i.e. for the case which had the largest intensity and scale). The resulting lift and drag correlations can be written in the following form:

$$C_{ff}^2(\tau, \zeta) = R_{ff}(\tau, \zeta)/q_m^2\, D^2, \tag{3}$$

where $C_{ff}(0, 0)$ is an r.m.s. force coefficient and f represents either lift or drag. Figure 9 shows the variation of $C_{ff}(0, \zeta)$ as a function of the lateral spacing ζ.

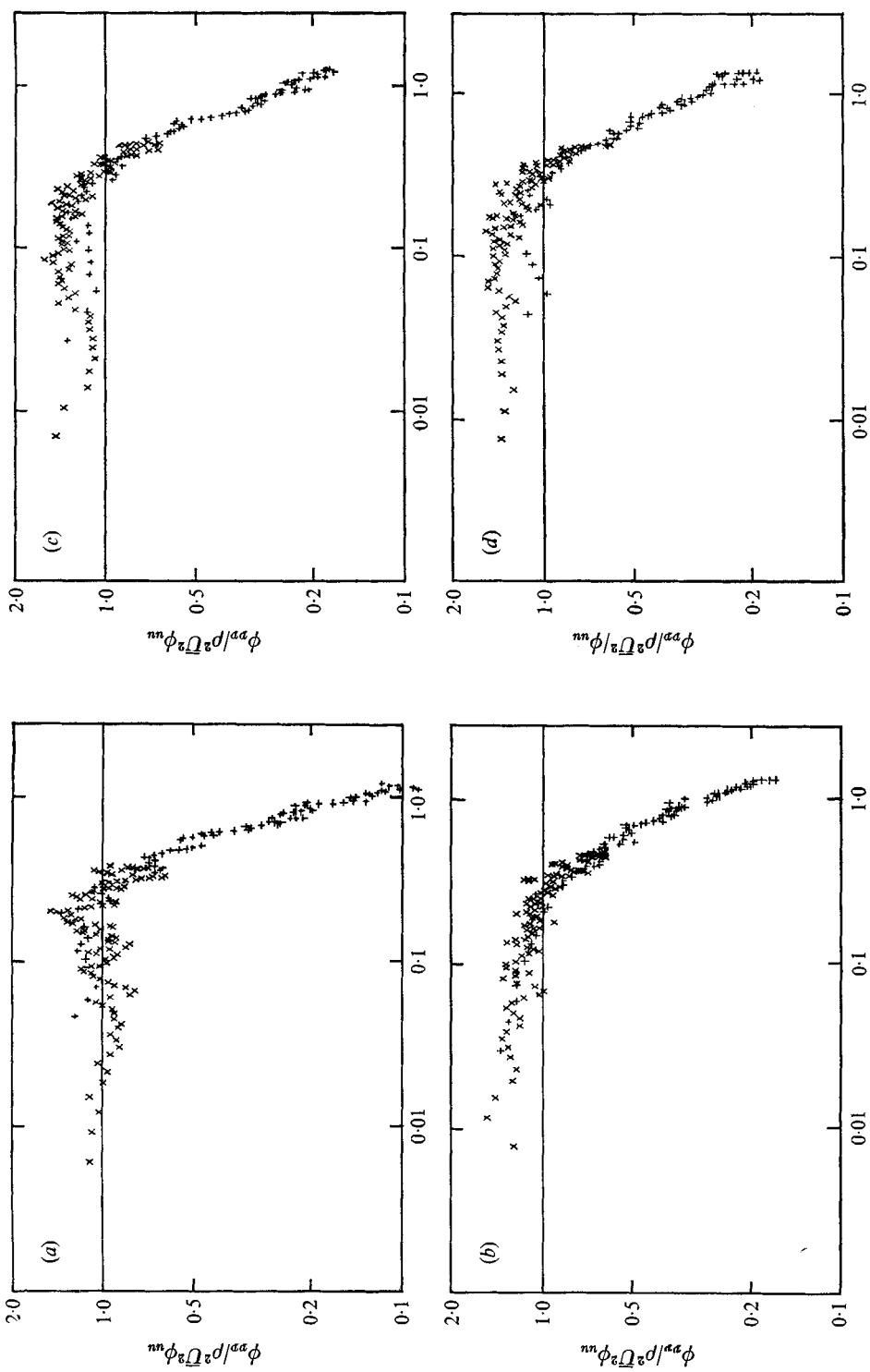

FIGURE 8. Pressure–velocity describing functions for the front stagnation point, (*a*) case 0, (*b*) case 1, (*c*) case 3, (*d*) case 4.

Two sets of results are shown: those derived from the first point of the time-delayed correlation data actually correspond to $C_{ff}(\frac{1}{2}\Delta\tau, \zeta)$ owing to the peculiarities of the PAR correlator; the other values were developed independently from real-time zero-lag pressure correlations formed on an analog computer. Neither set of data has been corrected for system frequency response as this is believed to be negligible in the integrated-force case. Since such corrections would

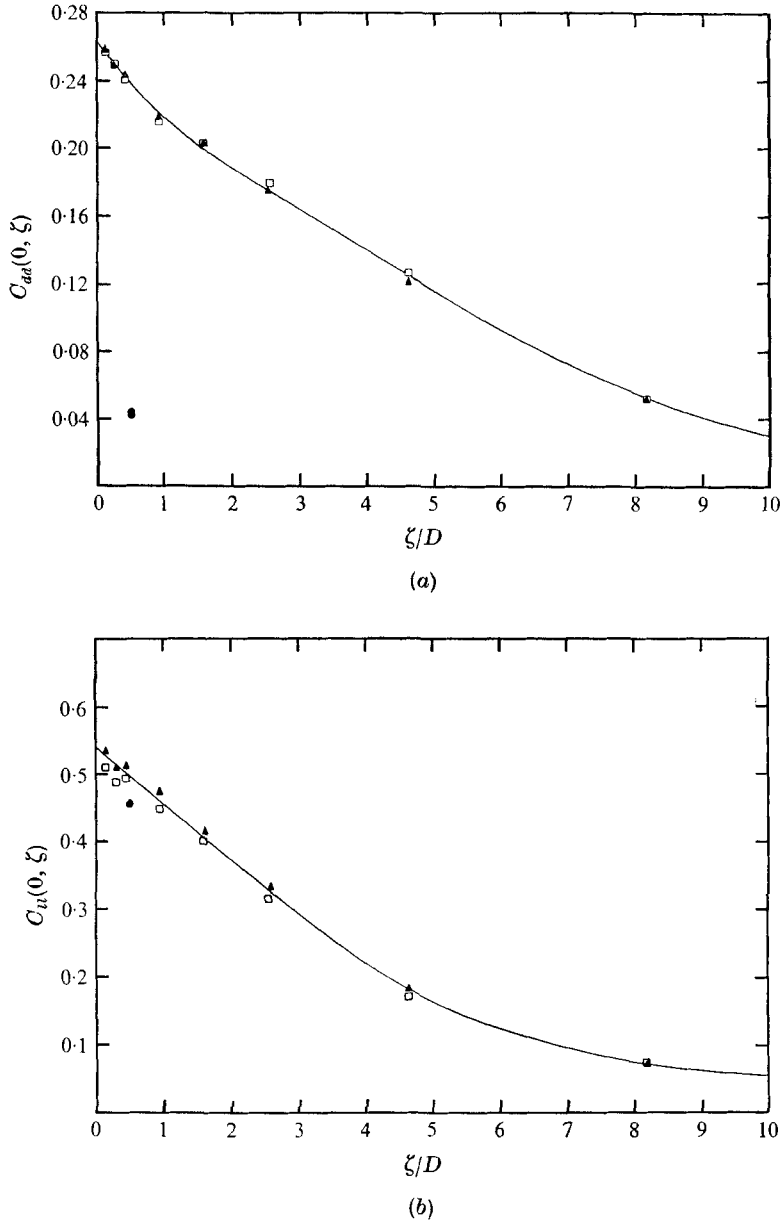

FIGURE 9. Variation of root force correlation coefficients with lateral spacing at zero time delay, (*a*) drag, (*b*) lift. □, PAR correlator output first point; ▲, analog computer results; ●, Keefe (1961).

actually be of opposite signs for the two cases (one was filtered and the other had the module resonance present), their agreement tends to verify this. Also shown are some previous results found by Keefe (1961) in smooth flow using a one-diameter long section of a cylinder as a force transducer. These results are plotted at $\tau/D = 0{\cdot}5$.

From figure 9 it can be seen that the fluctuating drag is roughly six times greater in this turbulence field than in Keefe's smooth stream. Hence the qualities of the input turbulence dominate the drag response. This is not the case for the lift response, as the values with and without turbulence are not significantly different, despite the probable change in the spectral distribution of the lift. The data of figure 9 (C_{ff}^2) can be integrated to yield force scales in lift of $2{\cdot}80D$ and in drag of $2{\cdot}31D$. Since these are similar to the lateral turbulence scale, found in this case as $Lu(y) = 2{\cdot}4D$, this suggests that the properties of the input turbulent flow tends to define the extent of the correlated pressures and forces along the cylinder.

Cross-spectra of the fluctuating lift and drag

Fourier transformation of the correlations yielded cross-spectral estimates of the lift and drag for the eight lateral spacings examined. The results are shown in figure 10, where the smooth curves represent best fits to the experimental data. The data points have been omitted for clarity but their details are discussed in Surry (1969). Generally, the curves are reliable descriptions of the behaviour of the experimental points except for the particular case of the drag cross-spectrum at minimum spacing. In this case the transformed data show a significant dip at the fundamental Strouhal frequency, where the data should be highly reliable. This has been considered an unexplained anomaly and disregarded since it does not occur at any other spacing and there does not appear to be a physical mechanism that satisfactorily explains it. It is possibly an error due to the integration of a number of data sets each subject to statistical uncertainties and small experimental errors. At the Strouhal frequency, the integrals of equation (1) should result in a large power spike in the lift direction, but these same pressure peak contributions ought to balance out in the drag direction. Obviously small errors at this point can lead to a relatively large drag anomaly.

This cross-spectral data serves to emphasize the domination of the lift response by the shedding, although the bandwidth is quite broad. As expected, the drag cross-spectra diminish rapidly with increasing lateral spacing and frequency. The physically possible fluctuating drag peak at twice the Strouhal frequency was not seen, and was presumably buried by the turbulence response.

Empirical drag response function

The simple theories of linearized response of line-like structures to turbulence such as presented by Davenport (1962) and Etkin (1966) lead to a transfer function for drag of the form

$$\frac{\phi_{dd}(f,\zeta)}{\rho^2 D^2 C_d^2 \overline{U}^2 \phi_{uu}(f,\zeta)} = 1 + 4\pi^2 \frac{k^2}{C_d^2}\left(\frac{fD}{\overline{U}}\right)^2, \tag{4}$$

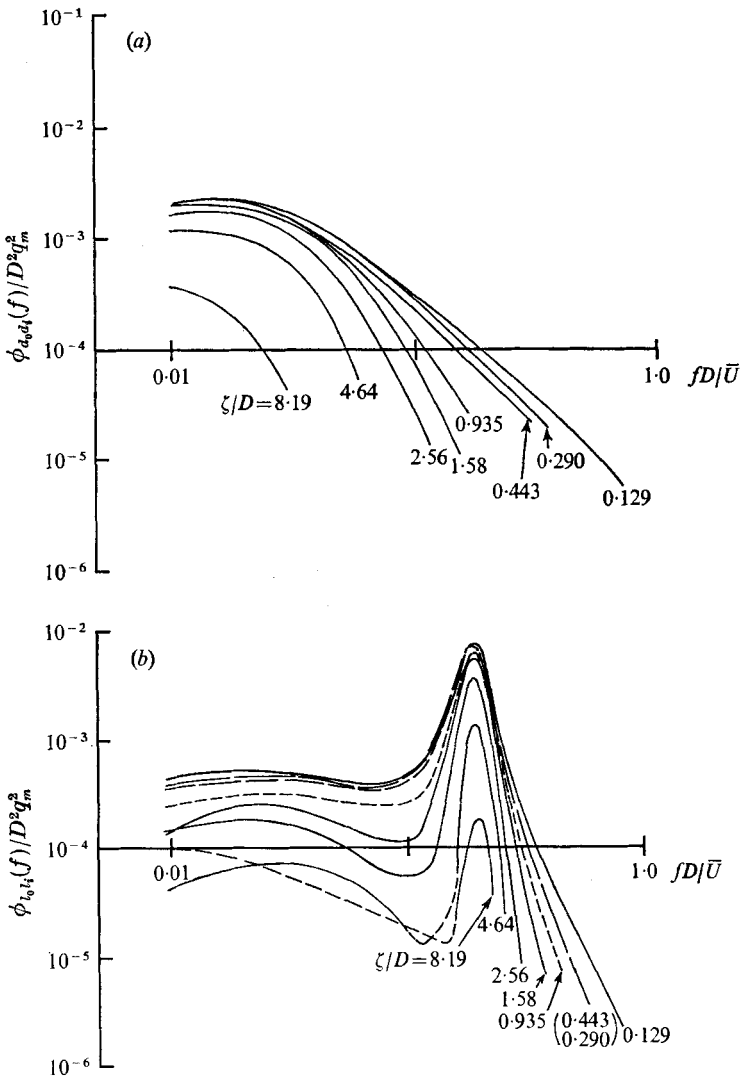

FIGURE 10. Smoothed experimental cross-spectra for eight lateral spacings, (*a*) drag, (*b*) lift.

where C_d is the experimental mean drag coefficient and k is the induced mass coefficient, usually taken as the theoretical value of $\frac{1}{4}\pi$. The experimental data plotted in this form are shown in figure 11, where the subscript '0' refers to the fixed module and i refers to the moveable module. It is immediately obvious that first, the data does not collapse as it should if a linear relationship is valid and second, that the addition of the acceleration, or induced mass term, does not provide a useful prediction – presumably because other attenuative features of the interaction (as seen for instance in § 5) dominate the response.

An alternative approach seeking a narrow-band collapse of the data was more successful. Previous work in the manner of Davenport (1962) on the collapse of

velocity cross-spectra had shown that for the frequencies of interest here, the velocity cross-spectra for case 4, could satisfactorily be described by the relation

$$\phi_{u_i u_0}/\phi_{u_0 u_0} = \exp\{-(6{\cdot}4\eta_i)^{1{\cdot}4}\},$$

where $\eta_i = f\zeta_i/\bar{U}$.† The drag data were examined seeking a similar collapse. Since $\phi_{d_0 d_0}$ was not available owing to the minimum distance prescribed by the experiment being $\zeta_1 = 0{\cdot}129D$, the ratio $\phi_{d_i d_0}/\phi_{d_1 d_0}$ was formed instead and plotted

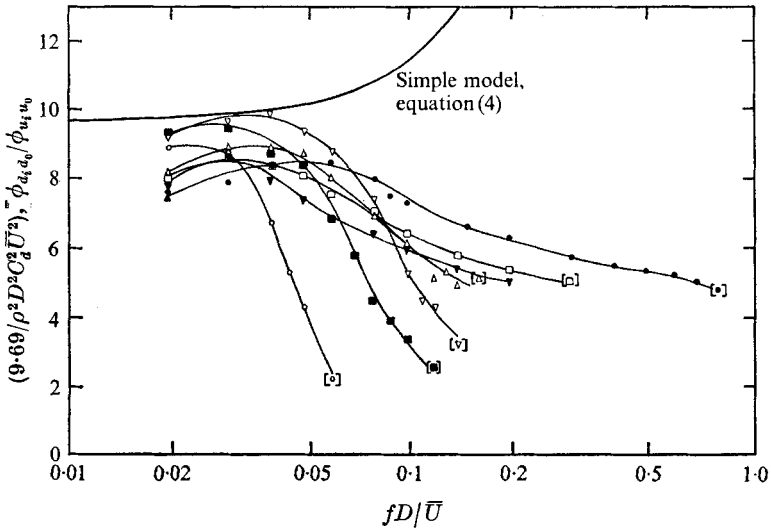

FIGURE 11. Simple describing function approach for the drag and u component of turbulence at the following ζ/D spacings: ●, 0·129; □, 0·29; ▼, 0·443; △, 0·935; ▽, 1·58; ■, 2·56; ○, 4·64; ▲, 8·19. [ ] indicates data at limit of reliability.

against $\eta_i' = (\eta_i^{1{\cdot}4} - \eta_1^{1{\cdot}4})^{1/1{\cdot}4}$ as shown in figure 12. The success of the collapse allowed a good fit to be established as

$$\phi_{d_i d_0}/\phi_{d_0 d_0} = \exp\{-(7{\cdot}9\eta_i)^{1{\cdot}4}\}.$$

Obviously the disparity in the decay constants for ϕ_{uu} and ϕ_{dd} is the reason for the lack of a linear collapse in ϕ_{dd}/ϕ_{uu} (figure 11). Instead it implies that the relationship between the drag and the u component of velocity for this case may be satisfactorily described by

$$\phi_{d_i d_0}/\phi_{u_i u_0} = |H(f)|^2 \exp\{-(d\eta_i)^{1{\cdot}4}\}, \tag{5}$$

where $d = [7{\cdot}9^{1{\cdot}4} - 6{\cdot}4^{1{\cdot}4}]^{1/1{\cdot}4} = 3{\cdot}0$ and $|H(f)|^2 = \phi_{d_0 d_0}/\phi_{u_0 u_0}$. Estimates of $|H(f)|^2$ were produced from the experimental values of $\phi_{d_i d_0}$ and $\phi_{u_i u_0}$ and (5) and are displayed in figure 13. There is considerable scatter in these results, however the mean behaviour has a consistent trend. None of the velocity spectra have been corrected for finite hot-wire length in this report. Application of Wyngaard's

† The form of collapse adopted here is a simplified form. A more general approach is given by Vickery (1965) and Harris (1970), who show that the collapsing parameter η is also a function of the longitudinal scale for a homogeneous isotropic turbulence. However, this is a weak effect for the frequencies considered here.

(1968) method indicates a possible correction of about 20 % at $fD/\overline{U} = 1{\cdot}0$ for the hot wires used here. This would only appreciably affect the data obtained from

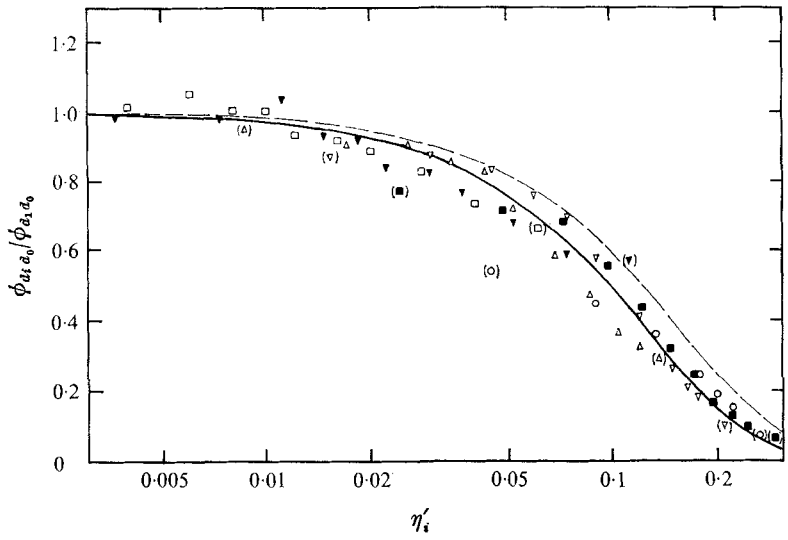

FIGURE 12. Normalized drag cross-spectral data. ——, $\exp\{-(7{\cdot}9\eta_i')^{1{\cdot}4}\}$; — —, $\exp\{-(6{\cdot}4\eta_i')^{1{\cdot}4}\}$, fit to velocity data; other notation as in figure 11.

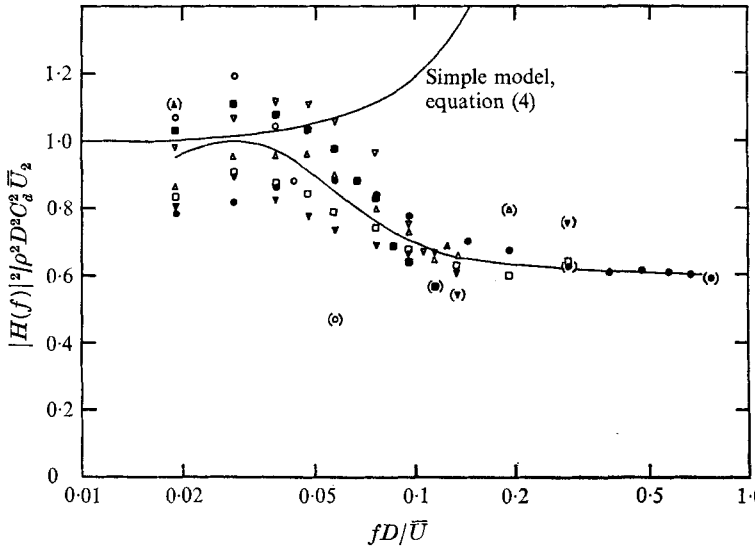

FIGURE 13. (Magnitude of the final drag)/(*u*-component describing function). Same notation as in figure 11.

the $\zeta/D = 0{\cdot}129$ case and would tend to reduce the value of $|H(f)|^2$ at high $fD/\overline{U}$. It would not, of course, affect the narrow-band collapses of the data.

Although relation (5) is a good approximation to the data obtained here, more work is required to establish whether its form is generally applicable. Since the exponential is essentially a fitting term for a nonlinearity, the value of d may be

a function of Re and turbulence characteristics. However it does provide an initial form for the drag cross-spectra in terms of the velocity cross-spectra, which is the primary relation required to determine structural response.

Empirical lift response function

Similar narrow-band cross-correlations were produced for the lift results and are shown in figure 14. These show the same sort of behaviour as the surface pressures at angles other than 0° in that each curve appears to be independent and shows

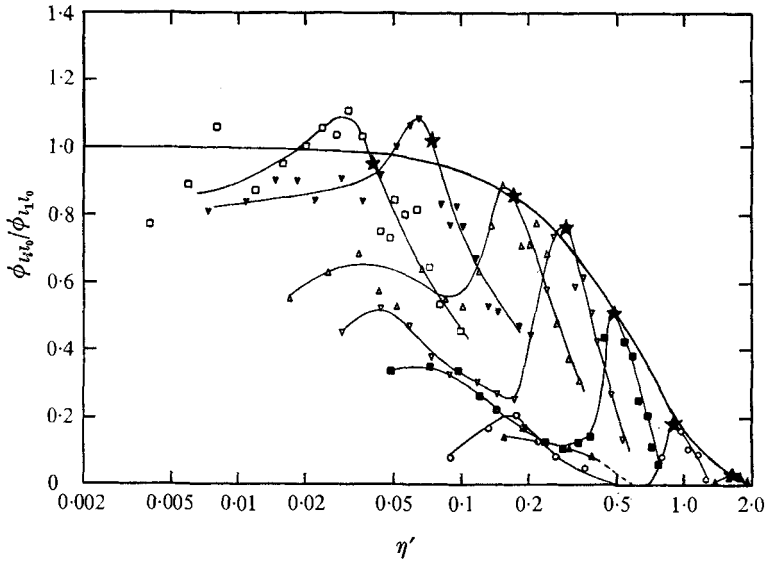

FIGURE 14. Normalized lift cross-spectral data. ★, Strouhal peak ratios; ——, $\exp\{-(1{\cdot}5\eta')^{1{\cdot}4}\}$; other notation as in figure 11.

a sharp rise in the region of the Strouhal frequency. The ascendancy of the peaks above unity occurs because of slight shifts in the position of the peak with ζ_i. Hence the actual peak ratios are indicated on the graph and are used to define an exponential fit given by

$$(\phi_{l_i l_0}/\phi_{l_0 l_0})_s = \exp\{-(1{\cdot}5 f_s \zeta/\overline{U})^{1{\cdot}4}\}.$$

The corresponding Strouhal lift scale is $3{\cdot}03D$.

The oscillating lift at very low frequency can be thought of as resulting from a slow change in direction of the velocity vector due to the cross-component w. In this quasi-steady case the low frequency linearized lift response would be simply related to the w component through the relation

$$\phi_{l_i l_0}/\phi_{w_i w_0} = \tfrac{1}{4}\rho^2 D^2 C_d^2 \overline{U}^2.$$

Since no w cross-spectra were measured, this relation could not be examined but the ratio $\phi_{l_1 l_0}/\phi_{w_0 w_0}$ was found to approach a value of about 1·3 times that suggested above, indicating that other sources of lift were also present. Of course, the relation is quite invalid as the vortex shedding region of the frequency domain is approached.

7. Concluding remarks

(i) Mean drag coefficients and vortex shedding frequencies measured in four turbulent fields are consistent with an effective increase in Re, which is determined both by the intensity and the scale of the turbulence. The measured values of $C_{\bar{d}}$ appear to be ordered logically when viewed in terms of the Taylor parameter, although it is not likely that this reflects the entire interaction.

(ii) At the Reynolds number examined, approximately 40 000, intense turbulence does not drastically disrupt the vortex shedding phenomena on a rigid circular cylinder. It remains to be shown how much of the changes that were reported are simply explained by an effective change in Re.

(iii) The effect of turbulence on the shedding phenomena appears to arise primarily from the low frequency spectral content – perhaps by wake interference – and serves mainly to broaden the Strouhal peak. The peak energy and lateral coherence is only slightly reduced by a severe turbulence with lateral scale of approximately $2{\cdot}4D$.

(iv) Under low turbulence conditions, surface pressure spectra in the range $\theta = 90$–$150°$ show small peaks at three times the Strouhal fundamental frequency.

(v) The spectra of drag and lift for approximately homogeneous turbulence with $\bar{u}/\overline{U} = 0{\cdot}147$ and $Lu(y)/D = 2{\cdot}4$ show that the fluctuating lift is still dominated by the broadened Strouhal peak, whereas the unsteady drag is primarily due to streamwise turbulence.

(vi) The data obtained here show that the commonly assumed acceleration, or additional mass term, is inappropriate and that in fact the drag response is not linearly related to the turbulent u component, but rather can be described by a slightly nonlinear relation of the form

$$\phi_{\bar{d}_i d_0}/\phi_{u_i u_0} = |H(f)|^2 \exp\{-(d\eta_i)^{1{\cdot}4}\},$$

where, here, d was found to be $3{\cdot}4$. It is not known how far this form is applicable to other turbulent fields.

This work was done under the supervision of Professor B. Etkin. Financial support was received from the National Research Council of Canada and from the U.S.A.F., R.T.D. under contract AF 33(615)-2305, of the Flight Dynamics Laboratory. The present paper was prepared at the National Physical Laboratory, Teddington, Middlesex.

REFERENCES

Bearman, P. W. 1967 *J. Fluid Mech.* **28**, 625.

Bearman, P. W. 1968 *Nat. Phys. Lab. Aero. Rep.* no. 1257.

Bearman, P. W. 1969 *J. Fluid Mech.* **37**, 577.

Bearman, P. W. 1970 *J. Fluid Mech.* **46**, 177–198.

Davenport, A. G. 1962 *Proc. Inst. Civ. Engrs.* **23**, 389–408.

Etkin, B. 1966 *Compilation of papers presented at Meeting on Ground Wind Load Problems in relation to Launch Vehicles, N.A.S.A. Langley Research Center.*

El Baroudi, M. Y. 1960 *U.T.I.A.S. Tech. Note*, no. **31**.

Fage, A. & Falkner, V. M. 1931 *Aero. Res. Coun. R. & M.* no. 1369.

HARRIS, R. I. 1970 *C.I.R.I.A. Seminar on the Modern Design of Wind-Sensitive Structures*, paper 3.

HINZE, J. O. 1959 *Turbulence*, p. 135. McGraw-Hill.

KEEFE, R. J. 1961 *U.T.I.A.S. Rep.* no. 76.

PRENDERGAST, V. 1958 *U.T.I.A.S. Tech. Note*, no. 23.

ROSHKO, A. 1961 *J. Fluid Mech.* **10**, 345.

SURRY, D. 1969 *U.T.I.A.S. Rep.* no. 142.

VICKERY, B. J. 1965 *Nat. Phys. Lab. Aero. Rep.* no. 1143.

WYNGAARD, J. C. 1968 *J. Sci. Instrum.* 1 (2), 1105–1108.